

Photonic Floquet time crystals

Bing Wang^{†,1}, Jiaqi Quan^{†,2}, Jianfei Han³, Xiaopeng Shen^{*,3}, Hongwei Wu^{*,2}, and Yiming Pan^{*,4}

1. National Laboratory of Solid State Microstructures and School of Physics, Nanjing University, Nanjing 210093, CHINA
2. School of Mechanics and Photoelectric Physics, Anhui University of Science and Technology, Huainan 232001, CHINA
3. School of Materials Science and Physics, China University of Mining and Technology, Xuzhou 221116, CHINA
4. Physics Department and Solid State Institute, Technion, Haifa 32000, ISRAEL

The public and scientists constantly have different angles on scientific issues. While on a time crystal, they stand in line and ask: “So, what is a time crystal? Show me a material that is automatic crystalline in time.” Here we reported a photonic material version of time crystals and experimentally observed its indicative period- $2T$ beating. We explicitly reconstructed a many-body Floquet ‘ground state’ for the discrete time-crystalline phase of matter from the single-particle picture, and experimentally revealed the rigid period-doubling oscillation, as a fingerprint of spontaneously breaking the discrete time-translational symmetry, in our well-designed photonic Floquet simulator. Different from the realizations enabled by the exquisite many-body interaction in trapped ions [1], diamond nitrogen-vacancy centers [2], superfluid quantum gases [3, 4] and nuclear magnetic resonances [5, 6], our photonic simulation of time crystals is radically derived from newly-defined single-particle topological states that can be extensively accessible to many pertinent non-equilibrium and periodically-driven platforms. We hope our observation of photonic time crystals can bring theoretical and technical interests to condensed matter physics and topological photonics, and also would willingly debunk the mystery of time crystals for the general public.

A time crystal is an exotic non-equilibrium phase of matter that spontaneously breaks the continuous or discrete time-translational symmetry. In the same manner, it mimics how an ordinary crystal in space spontaneously breaks its spatial translation symmetry when cooling down in temperature. In 2012, Frank Wilczek first proposed the concept of time crystals in both classical and quantum versions [7-9], but in the following, the original time-crystalline model was proved to be invalid in static equilibrium and later ruled out by a no-go theorem [10, 11]. While breaking the discrete time-translational symmetry in periodically-driven systems is not ruled out [12-15], and even points us in a promising direction of research [16-19]. To date, most of the materialized time crystals follow this path and explore rapidly in quantum simulation platforms [1-6, 20-25]. Still, the ‘ground state’ (a state of minimum energy) of a genuine time crystal is elusive because it is intrinsic out-of-equilibrium after broken spontaneously.

Usually, the existence of an automatic time-crystalline phase can be assessed by probing a stable subharmonic response in experiments, such as period-doubling (with twice the periods of the underlying drive). However, time crystals are not the only materials or systems that can give rise to subharmonic period- $2T$ oscillation [18, 26, 27]. Indeed, even before the inception of the discrete time-crystalline phase the period- $2T$ oscillations have been widely studied in a variety of classical and quantum systems, such as the period-doubling bifurcation from the logistic map [26], the subharmonic response in the chaotic [28-30] or dissipative [20, 31, 32] systems, and the coupled nonlinear parametric oscillators (e.g., Van der Pol oscillator) [27, 30]. Moreover, there are many fascinating candidates of time-crystalline systems that recently sprang up [3, 33-37]. That is to say, the crucial subharmonic evidence to experimentally examine a time-crystalline phase seems disputable.

To further address the debate, we can ask a following question: is the time-crystalline phase of matter a single-particle excitation, a many-body collective phenomena, or a chaos-induced dynamical behavior? No answer has been uniquely confirmed. To explore the genuine phenomena of time crystals, indeed, more experiments are calling. Hence, this paper explores how to construct a single-particle picture of time crystals that enables the rigid period- $2T$ oscillation [38]. Inspired by great successes in the discoveries of topological insulators and topological photonics [43-47], here, we would like to realize a robust photonic Floquet time crystal to facilitate the development of topological periodically-driven time-crystalline orders.

Our observation indicates a universal presence of Floquet time-crystalline phases in topological materials and systems [24, 25, 38].

Let us firstly formulate an analytical expression to elucidate the ‘ground state’ of a Floquet or discrete time-crystal (FTC, or DTC). To give an illustration on a spin chain, as we schematically shown in Fig. 1a, a many-body-localization-enabled time-crystalline state (i.e., π -spin glass) is intensively studied [13-15, 48], given by $|\{\pm\}\rangle = (|\uparrow\downarrow\uparrow\uparrow\downarrow\uparrow\cdots\rangle \pm |\downarrow\uparrow\downarrow\downarrow\uparrow\downarrow\cdots\rangle)/\sqrt{2}$. Notably, the spin-glass states $|\{\pm\}\rangle$ are the eigenstates of Floquet evolution operator: $U_F|\{\pm\}\rangle = e^{-i\epsilon_{\pm}T}|\{\pm\}\rangle$, and consequently, the period-doubling is expected due to the energy splitting $|\epsilon_+ - \epsilon_-| = \pi/T$ with T the driving period. This fully-entangled many-body ‘ground state’ is dubbed as π SG/DTC (π -spin glass/discrete time crystal) [15]. By imitating the π SG/DTC Floquet states, we can conjecture a many-body Floquet product state, suggested as

$$|\Psi_{FTC}\rangle = |edge\ state\rangle \otimes |DW\rangle \otimes |DW\rangle \otimes \cdots |DW\rangle \otimes |edge\ state\rangle, \quad (1)$$

where the edge state $\left(\sim \frac{|\uparrow\rangle \pm |\downarrow\rangle}{\sqrt{2}}\right)$ is the disorder-protected quantum order at ends, and the domain walls (DWs) $\left(\sim \frac{|\uparrow\downarrow\rangle \pm |\downarrow\uparrow\rangle}{\sqrt{2}}\right)$ are protected local integral of motions (LIOMs) randomly distributed on the chain [18, 48-50]. Thus, the constructed many-body time-crystalline state (Eq. 1) consists of the direct product of these local single-particle topological edge states and domain walls, as shown in Fig. 1b.

Consider a topological Floquet phases [51-53], holding both 0- and π -quasienergy modes at ends or in kink structures [38-42]; therefore correspondingly, the edge-state and DW excitations can be described as the superposition states of two topological modes, i.e.,

$$|edge\ state\rangle = \frac{|0\rangle \pm |\pi\rangle}{\sqrt{2}}, |DW\rangle = \frac{|0DW\rangle \pm |\pi DW\rangle}{\sqrt{2}}. \quad (2)$$

As shown in Fig. 1b, there presents a period- $2T$ beating as a result of the superposition of zero ($|0\rangle, |0DW\rangle$) and π quasi-energy eigenstates ($|\pi\rangle, |\pi DW\rangle$). The dynamic intensity of a local superposition Floquet state is prototypically given by $I_{\pm}(x, t) = |\psi_0(x, t) \pm \psi_{\pi}(x, t)|^2 = |\psi_0(x, t)|^2 + |\psi_{\pi}(x, t)|^2 \pm 2\Re\{\psi_0^*(x, t)\psi_{\pi}(x, t)\}$. From the Floquet-Bloch theorem [54, 55], the two Floquet eigenstates are given by $\psi_{0,\pi}(x, t) = u_{0,\pi}(x, t)e^{-i\epsilon_{0,\pi}t}$, where $u_{0,\pi}(x, t) =$

$u_{0,\pi}(x, t + T)$ defines the micromotion within one cycle and $\epsilon_{0,\pi}$ are the corresponding quasienergies, respectively. Therefore, the intensity of the superposition is obtained as

$$I_{\pm}(x, t) = |u_0(x, t)|^2 + |u_{\pi}(x, t)|^2 \pm 2\Re\{u_0^*(x, t)u_{\pi}(x, t)\} \cos(|\epsilon_0 - \epsilon_{\pi}|t). \quad (3)$$

The period-doubling occurs if the quasienergy difference $|\epsilon_0 - \epsilon_{\pi}| = \pi/T$ is fixed. We can check the relation $I_{\pm}(x, t + 2T) = I_{\pm}(x, t)$, so that the intensity evolves with a double period of the drive, as shown in Fig. 1c. Namely, the $2T$ -periodic subharmonic response comes from the interference between the symmetry-protected Floquet eigenmodes. Two aspects are worth mentioning here. First, it is not difficult to pick two quasienergy states with the splitting π/T in the Floquet-Brillouin zone $(-\frac{\pi}{T}, \frac{\pi}{T})$, and realize the period- $2T$ beating. However, the problem is that this kind of subharmonic response is sensitively fragile since it would be destroyed by an infinite small perturbation. The vulnerability of this period-doubling made up its excuse: the energy splitting can be quickly affected by other Floquet quasi-eigenstates, and the period- $2T$ interference (the 3^{rd} term in Eq. 3) is assuredly perturbed. With this issue of stability in mind, only the nontrivially-gapped Floquet modes are robust against any further perturbation or disorder [38, 42].

The second aspect is that the relevant subharmonic interference has to be local, that is, $2\Re\{u_0^*(x, t)u_{\pi}(x, t)\} \neq 0$, and thus, the 0- or π - edge states and domain walls are located at the same ends or kink structures. Whereas the different micromotions of 0 and π modes are faraway to overlap, yielding to no interference. So, only the local superposition (between 0 and π modes) can predominantly contribute to the emergent $2T$ -periodic oscillation.

Setup - Our modeling of photonic FTC is easily set up based on the known Su-Schrieffer-Heeger (SSH) model for Polyacetylene (1979) [56], which has been widely investigated in many photonic simulation platforms (e.g., [46, 47]). The edge states and domain walls can be constructed in a driven SSH model for electrons (Fig. 1d) [38]. For easily implementation in photonic systems, we choose the periodically-driven SSH chain, and the Hamiltonian of this biatomic model is given by $H(t) = \sum_{i=1}^{N-1} [\kappa_0 + (-1)^i(\delta\kappa_0 + \delta\kappa(t))]c_i^{\dagger}c_{i+1} + h.c.$, where $c_i^{\dagger}(c_i)$ are the creation (annihilation) operators of the light field amplitude on the i^{th} waveguide.

The time-periodic coupling term between two nearest-neighboring waveguides (or sites) is dimerized, $\kappa_{i,i+1}(t) = \kappa_0 + (-1)^i(\delta\kappa_0 + \delta\kappa(t))$, where κ_0 is the constant coupling strength, $\delta\kappa_0$ is the time-independent staggered coupling strength due to the global dimerization, and $\delta\kappa(t)$ is the time-dependent staggered coupling strength due to the time-periodic dimerization, for our structural consideration, which is given by $\delta\kappa(t) = \delta\kappa_1 \cos(\omega t + \theta)$ with $\delta\kappa_1$ being the strength of the coupling and $\omega = 2\pi/T$ the Floquet driven frequency and θ the initial phase (Floquet gauge) of the drive. Equivalently, the topological phases in the driven SSH model can be mapped into the transverse field Ising model [18, 38, 40] or the Kitaev model for p-wave superconductor [24, 38, 39, 41, 42].

In our experiment, the periodic coupling $\kappa_{i,i+1}(t)$ is fully designed and controlled by the spatial spacing (G) between two neighboring curved waveguides. As schematically shown in Fig. 1d, a photonic simulator of driven SSH chain is designed by mapping the evolution time t of an electron into the propagation direction z of the light, and correspondingly, mapping the Floquet cycle T into the curving period Λ . So, the coupling profile is given by $\kappa_{i,i+1} = \kappa_{i,i+1}(G, \Lambda)$. For demonstration, we define an effective coupling length $l_c = \pi/2\kappa_0$ of our simulator in order to compare with the period Λ , and require the dimerization conditions $\delta\kappa_0 \ll \kappa_0, \delta\kappa_1 \ll \kappa_0$ for the further fabrication. Typically, the coupling length l_c is in a range of (20 mm, 100 mm) and the curving period is fixed to $\Lambda = 100$ mm. The coupling profiles extracting from simulations can be found in the SM file.

Quasi-energy gap opening - Figure 2 demonstrates the quasienergy band for the emergent topological phase coexistence of both zero and π Floquet modes. The quasienergy spectrum is precisely calculated using the eigenvalue problem analyses of the Floquet Hamiltonian $H_F = \frac{i}{\Lambda} \exp\left(-i \int_0^\Lambda H(z) dz\right)$, in which the Hamiltonian is time-periodic $H(z) = H(z + \Lambda)$. Fig. 2a presented the desired band as a function of the Floquet cycle (Λ), in comparison with the effective coupling length (l_c). With taking into account both the dimerizations ($\delta\kappa_0 \neq 0, \delta\kappa_1 \neq 0$), the coexistence of two Floquet modes occurs at the periodically-curving condition $\Lambda/l_c \in (1, 2)$, associating with two quasienergy gap invariants [53] (see the Method).

Correspondingly, in the coexistence region, the eigenstates of 0 and π modes are demonstrated in Fig. 2b. We plotted their evolution patterns in four cycles ($4T$), showing that both two Floquet modes are periodic in T . The intensity of 0 mode is mainly localized on the first

waveguide of the boundary of the array. The π -mode propagates along with the first two waveguides periodically. Notably, the sole eigenstate excitation of either 0 modes or π modes cannot produce the period-doubling oscillation.

Figure 2c and 2d demonstrate the dependence of 0- and π -gap opening on the staggered strengths $\delta\kappa_0$ and $\delta\kappa_1$, respectively. At a fixed cycle in the Floquet coexistence region, the 0- and π -gap closed at $\delta\kappa_0 = 0$ and $\delta\kappa_1 = 0$, separately, as schematically shown in the insets, and then linearly opens as the dimerization strengths increase. There is a difference that the 0 mode would disappear at $\delta\kappa_0 < 0$ (corresponding to a trivial phase), while the π mode still exist at $\delta\kappa_1 < 0$. The reason is that, for the negative periodic staggered coupling strength, we notice that $-\delta\kappa_1 \cos(\omega t + \theta) = \delta\kappa_1 \cos(\omega t + \theta + \pi)$ corresponds to the π -phase shift for a Floquet gauge choice. That is to say, the π modes emerging with the negative dimerization coupling ($-\delta\kappa_1$) and gauge (θ) are equivalent to the modes with the positive dimerization coupling ($+\delta\kappa_1$) and gauge ($\theta + \pi$). At the moment, we can declare the advantage of our array design, that is, the global dimerization solely controls the opening of 0-gap, and the time-period dimerization solely controls the opening of π -gap. This dependence allows a considerable convenience to control and to demonstrate our theoretical expectation with the photonic simulation and measurement.

Period- $2T$ beating in photonic Floquet simulator - Our photonic simulator is made up of the coupled ultrathin corrugated copper strips that support spoof surface plasmon polaritons (SPPs) propagating at microwave frequencies as the guided wave highly-confined on a plasmonic waveguide. These ultrathin microstrip lines were proposed by [57, 58] and have been recently implemented as a simulation platform to observe anomalous topological modes [59]. These ultrathin waveguides deposited on a flexible dielectric substrate (F4BK) that can be bent, folded, coiled and even twisted to guide the spoof SPPs [57, 60]. Prior to the array fabrication, we used a finite element method implemented in the commercial software to numerically simulate the near-field field distribution of the TM-polarized wave (perpendicular to the ultrathin metallic waveguide interface) propagating along the z-direction on our array. The details of fabrications, measurements and simulations see the Method.

Figure 3 compares the theoretical expectation, numerical simulation, and experimental observation of the stroboscopic evolutions of the topological 0π -superposition. As we experimentally observed in Fig. 3c, the $2T$ -periodic oscillation was manifestly probed on the

driven SSH array sample, in perfectly agreement with our prediction (Fig. 3a) and simulation (Fig. 3b). The array consists of ten curved waveguides ($N = 10$) with period length (Floquet cycle) $\Lambda = 100 \text{ mm}$, has a total length $L = 400 \text{ mm}$. Its structural fabrication mimics the periodically driven SSH model taking into account both global and time-periodic dimerizations. The experimental near-field intensity pattern was scanned by a metallic tip to detect the electric field (E_z) over the simulator surface, which connects with a network analyzer to collect and perform the near-field distribution imaging (see the Methods).

With the coupling profiles corresponding to the structural parameters in mind, we calculated the dynamical evolution from the first waveguide of the array. Fig. 3a showed the intensity distribution within four Floquet cycles ($4T$), demonstrating the period- $2T$ oscillation twice along the array's boundaries. As we can see from the quasi-energy band, the input field was mainly projected into the chiral-symmetry-protected edge modes ($|\psi_{in}\rangle = \alpha|0\rangle + \beta|\pi\rangle$). After experiencing N Floquet cycles, the stroboscopic dynamics of the superposition is then given by $U_F(nT)|\psi_{in}\rangle = \alpha|0\rangle + (-1)^n\beta|\pi\rangle$. Thus, the resultant period doubling appears because the period number (n) must be even, for returning its initial superposition state ($|\psi_{in}\rangle$).

Many-body versus single-particle time crystals - The time-crystalline subharmonic response appears on the boundaries of a chain, and as well can emerge in the bulk as domain walls (as the interface modes between Floquet phases). To mimic a many-body Floquet time-crystalline phase (Eq. 2), here we designed an interesting Floquet simulator with DWs and edge states,

$$|edge\ state\rangle \otimes |DW\rangle \otimes |edge\ state\rangle.$$

As depicted in Fig. 1d, the two Floquet edge states lie at two ends, and a domain wall (DW) is placed at the middle of the array. Indeed, the existence of DWs only depends on the global topological difference of both sides [38], while free from the local coupling configuration. The principle of bulk-edge correspondence supports the DW excitations [43]. To retain the structural symmetry of our photonic simulator, the middle waveguide is set to be straight (Fig. 4a). Nevertheless, the local central couplings to the lopsided curved waveguides are still periodic. We address that both the end states and domain walls allow the coexistence of the two anomalous Floquet modes in our design.

Figure 4b-4d demonstrates the simulated field distributions of many-body time-crystalline states with three inputs: the central DW, two end states, and their combination. The input

frequency is 17.0 GHz, the array length is as same as 400 mm and divided into four cycles, the waveguide number is increased up to $N = 15$ with a central straight waveguide on the 10th site to hold the DW. In our simulation, the field distribution propagates along the waveguides oscillating with a period twice that of the curving. The local period-doubling behavior is rigid owing to the spatial separation of these topological excitations, so that it does not suffer from the finite-size hybridization. To reasonably extend, we should be able to observe a many-body time-crystalline oscillation by adding randomly-distributed but adequately-separated DWs in our Floquet simulator.

To explain the many-body product state dephasing into the fully-entangled state, we should take into account the kink-kink interactions between DWs [61]. This kink interaction represents the renormalized exponentially-decay interactions between local integrals of motions in the context of many-body localization [49, 50]. Then we can expect a modest kink-kink scattering to fade the product many-body state (Eq. 1) into an entangled state, rather than violating the local DW excitations

$$|\Psi'_{FTC}\rangle = \frac{|\dots \uparrow\downarrow\uparrow\uparrow\downarrow \dots\rangle \pm |\dots \downarrow\uparrow\downarrow\downarrow\uparrow \dots\rangle}{\sqrt{2}}, \quad (4)$$

where these local ‘spins’ are effectively defined as $|\uparrow\rangle = (|0DW\rangle + |\pi DW\rangle)/\sqrt{2}$, $|\downarrow\rangle = (|0DW\rangle - |\pi DW\rangle)/\sqrt{2}$ (Eq. 2). This many-body state is an example that all local topological excitations are fully entangled. It can directly compare with the many-body-localized-enabled π SG/DTC state [13-15]. Here, we suppressed the notation of edge states at ends in Eq. 4, which resemble the disorder-induced quantum order in MBL phase [50]. In light of the spatial confinement characteristics of the entangled Floquet modes, only the local zero and π modes superposition in the effective spins permits the subharmonic interference (Eq. 3). Therefore, the fully-entangled state $|\Psi'_{FTC}\rangle$ also experiences an indicative ‘fingerprint’ period- $2T$ oscillation. For a photonic realization, mimicking the many-body entanglement requires the optical nonlinearity of the waveguides [62]. It exceeds the capability of our Floquet simulator because the nonlinearity in the spoof plasmonic waveguides is negligible [57, 58]. With this material limitation in mind, we realize it is difficult to demonstrate the entangled state in our simulators. To be honest, we leave this issue open for future exploration in other quantum platforms [1-6].

Topological Floquet phase transition - Take a close look at the quasienergy band out of the coexistence region (Fig. 2a), we find that only zero-modes survive at high-frequency driven region $\Lambda/l_c \in (0, 1)$, and only pi-mode appear at the intermediate region $\Lambda/l_c \in (2, 3)$. By decreasing the curving period, one can expect a sequent harmonic (period- T), subharmonic (period- $2T$), and static responses on the boundaries because the corresponding Floquet system undergoes a phase transition from pi modes, topological phase coexistence, and zero modes [38]. From the perspective of sample fabrication, we have much practice and direct trick to detect this transition feature by means of altering the ratio between the global and periodic dimerizations.

Figure 5 demonstrates the experimental near-field observation of the topological transition from a T -periodic, $2T$ -periodic, and to static response. Fig. 5a corresponds to the π -mode excitation, compared with the case $\delta\kappa_0 = 0$ in Fig. 2c. Then, we increase a global staggered distance between two neighboring waveguides. The zero-modes emerge due to the nontrivial 0-gap opening via increasing global dimerization. Likewise, Fig. 5b shows a period- $2T$ subharmonic evolution due to the coexistence. Finally, in the nearly full dimerization limit (corresponding to the hardly coupling between the first two waveguides), only the first waveguide can propagate the input field, indicating that the extremely isolated zero mode exists but pi mode is suppressed. As shown in Fig. 5c, the most field intensity stays on the first waveguide demonstrating the dominant zero-mode evolution. Still, few input field diffuses into the array owing to the effective surplus of the remaining coupling between waveguides. Besides, we thoroughly investigate the dependence of Floquet cycles and that of input frequencies, which can be found in the SM file.

Conclusion - In short, we designed a photonic material version of Floquet time crystal and observed its prototypical period-doubling behavior in our well-designed Floquet simulators. To avoid many-body interaction in our photonic simulation, we reconstructed a non-interacting topologically-protected time-crystalline state composed of Floquet topological edges states and domain walls. For the first time, both the single-particle and many-body pictures of discrete time-crystalline phases are proposed and demonstrated. We believe the non-interacting topological Floquet time crystals can be easily extended for implementation in many classical and quantum platforms. Also, we hope our photonic Floquet time crystal can shed light on exploring exotic time-crystalline orders, and trigger further development of the out-of-equilibrium phase of matter in photonics and condensed matters.

Acknowledgement

This work was supported in part by DIP (German-Israeli Project Cooperation) and by I-CORE Israel Center of Research Excellence program of the ISF, and by the Crown Photonics Center, and also was supported by National Natural Science Foundation of China (NSFC) (Grants No. No. 11904008), National Natural Science Foundation of China (61372048), and the Six Talent Peaks Project in Jiangsu Province of China (XYDXX-072).

Author contributions

Y. P. and B. W. proposed the concept and modeling. J. Q. and H. W. contributed to the numerical simulation, design, and setting of the experiment. J. H. and X. S. performed the sample fabrication and near-field measurement and analyzed them all together with others. YP drafted the manuscript with all authors' contributions to the writing.

B. W. and J. Q. contributed equally to this work.

Corresponding authors

Correspondence to Yiming Pan, Hongwei Wu, and Xiaopeng Shen

Competing interests

The authors declare no competing interests.

Methods

1. Sample fabrication, setup and near-field measurement

The sample was fabricated in a printed circuit board (F4BK) with dielectric constant 2.65, loss tangent 0.001, and thickness 0.2 mm, the copper film thickness is 0.018 mm, and the total length of the array is 400 mm. Took consideration for eliminating reflections, and we added 50 mm at the begin of the waveguide lattices for ground lines. To assess our array design, we fabricated several examples with different sizes and measured the field pattern distribution using a near field scan system. Using a standard printed circuit board manufacturing process, several types of waveguide arrays are printed on the same dielectric substrate with a curving period $\Lambda = 100$ mm, $G_{min1} = 0.9$ mm, $G_{min2} = 0.9$ mm (for only π modes), and $\Lambda = 100$ mm, $G_{min1} = 1.9$ mm, $G_{min2} = 0.9$ mm (for both 0 and π modes). The spacing profiles see the following section. Note that G_{min1} is the minimal spacing between the first and second curved waveguides in the array, and G_{min2} is the minimal spacing between the second and third curved waveguides.

Near-field scanning technology is used to map the electric field over the sample surface. The experimental devices used include the vector network analyzer (KeysightE5063A), the translation platform, the two-dimensional platform controller, the detector, and the coaxial transmission line (Fig. S1 of the SM file). The sample is pasted on a foam that is larger than the array, and the foam is placed on the movable platform bottom plate. The bottom plate can move in two directions, X and Y , and is controlled by a two-dimensional platform controller, and the step length is set to 0.1 mm. One port of the vector network analyzer is connected to the feed coaxial line to provide the microwave source signal. The other port is connected to the coaxial detection probe. The probe is fixed on the fixed frame, and the inner conductor of the monitoring probe extends 1 mm, so as to observe the Z component of the electric field in the plane 1 mm above the sample. A specific computer program can analyze the near-field information, which is compared with the simulations. The test results show that in the near-field distribution of E_z component, for sample 1 with $N = 4$, $G_{min1} = 0.9$ mm, and $G_{min2} = 0.9$ mm, the simulation and measurement results are in excellent uniformity, and a T -periodic π mode propagation appears. For sample 2 with $N = 4$, $G_{min1} = 1.9$ mm, and $G_{min2} = 0.9$ mm, a period- $2T$ oscillation behavior appears (see Fig. 3).

2. Numerical simulations

To verify our theoretical prediction, we conduct full-wave simulations for TM-polarized waves propagating along the z -direction based on finite element analysis with *COMSOL Multiphysics*. The spoof plasmonic waveguide arrays in microwave regime are printed on a dielectric substrate F4BK with the parameters, the thin spoof plasmonic waveguides made of the copper strip with thickness is 0.3 mm , and the total length of the array is $L = 400 \text{ mm}$. The parameters of the structural unit cell (“H”-bar) are given by $P = 2 \text{ mm}$, $H = 4 \text{ mm}$, $a = 0.8 \text{ mm}$, $W = 1 \text{ mm}$, see the Fig. S1. The biatomic spoof plasmonic waveguides are designed conforming to the relation $G(z) = g_0 \pm g_1 \pm 2A_0 \cos(2\pi z/\Lambda + \theta)$, where g_0 is the averaged spacing between waveguides, g_1 is the global dimerization spacing. Also, $A_0 = 0.8 \text{ mm}$ is the fixed z -periodic dimerization spacing with the period Λ and the initial phase θ , which is cosine-modulated in the propagation direction z . The coupling length $l_c = \pi/2\kappa_0$ and coupling strength κ_0 as a function of the spacing is simulated, as shown in Fig. S2.

Particularly, to simulate the time-crystalline period- $2T$ beating with the array dimerization of spoof plasmonic waveguides, we set the minimum internal spacing of two adjacent waveguides, $(G_{min1}, G_{min2}) = (0.9 \text{ mm}, 0.9 \text{ mm})$ for only time-periodic dimerization, corresponding to $g_0 = 2.5 \text{ mm}$, $g_1 = 0$, $A_0 = 0.8 \text{ mm}$, and $(G_{min1}, G_{min2}) = (1.9 \text{ mm}, 0.9 \text{ mm})$ for both the global and periodic dimerization, corresponding to $g_0 = 3.0 \text{ mm}$, $g_1 = 0.5 \text{ mm}$, $A_0 = 0.8 \text{ mm}$. The total number of bending periods (Floquet cycles) within L is set as $N = 4$ for all waveguides. The drive signal with frequency 17.0 GHz is input from the first waveguide in our simulation. The boundaries of the whole array structure are defined as the scattering boundary condition.

3. Theoretical calculations

Mapping 1/2-spin chain to SSH chain - The one-dimensional $1/2$ -spin chain system studied in the π SG/DTC phase [18] is given by

$$H = - \sum_{i=1}^{N-1} J_i(t) \sigma_i^x \sigma_{i+1}^x - \sum_{i=1}^N h_i(t) \sigma_i^z + J_z \sum_{i=1}^{N-1} \sigma_i^z \sigma_{i+1}^z. \quad (\text{M1})$$

For simplification, we suppose to average the disorders and time-periodicity, and consider the small interaction term,

$$\bar{J} = \langle\langle J_i(t) \rangle\rangle, \bar{h} = \langle\langle h_i(t) \rangle\rangle, \text{ and } J_z \ll \bar{J}, \bar{h}. \quad (\text{M2})$$

If $\bar{J} > \bar{h}$, the first term is dominating which leads to a Z_2 breaking ferromagnetic phase (FM) (i.e., spin glass, at $J_z \neq 0$), while if $\bar{J} < \bar{h}$, the second term is dominating which leads to a paramagnetic phase (PM). The critical point at $\bar{J} = \bar{h}$ corresponds to the FM-PM phase transition.

Let us perform the Jordan-Wigner transformation

$$\sigma_i^+ = 2 \exp \left[-i\pi \sum_{k=1}^{i-1} c_k^\dagger c_k \right] c_i^\dagger, \sigma_i^- = 2 \exp \left[i\pi \sum_{k=1}^{i-1} c_k^\dagger c_k \right] c_i, \quad (\text{M3})$$

where $\sigma_i^\pm = \sigma_i^x \pm i\sigma_i^y$ are the raising and lowering operators, c_i^\dagger, c_i are the creation and annihilation operators of fermions at the site i . Via the transformation (M3), we map the spin chain to a p -wave pairing superconductor with near-nearest Coulomb interaction

$$\begin{aligned} H = & - \sum_{i=1}^{N-1} J_i(t) (c_i^\dagger - c_i) (c_{i+1}^\dagger + c_{i+1}) - \sum_{i=1}^N h_i(t) (2c_i^\dagger c_i - 1) \\ & + J_z \sum_{i=1}^{N-1} (2c_i^\dagger c_i - 1) (2c_{i+1}^\dagger c_{i+1} - 1). \end{aligned} \quad (\text{M4})$$

Furthermore, the Dirac fermionic creation and annihilation operators c_i^\dagger and c_i can be written as the Majorana operators $c_i = \frac{1}{2}(\gamma_{2i-1} - i\gamma_{2i}), c_i^\dagger = \frac{1}{2}(\gamma_{2i-1} + i\gamma_{2i})$. It is easy to verify that the Majorana fermions satisfy the relations $\gamma_i = \gamma_i^\dagger, \{\gamma_i, \gamma_j\} = 2\delta_{i,j}$. Thus, we express the spin Hamiltonian (M1) in terms of Majorana fermions,

$$H = -i \sum_{i=1}^{N-1} J_i(t) \gamma_{2i} \gamma_{2i+1} - i \sum_{i=1}^N h_i(t) \gamma_{2i} \gamma_{2i-1} - J_z \sum_{i=1}^{N-1} (\gamma_{2i} \gamma_{2i-1}) (\gamma_{2i+2} \gamma_{2i+1}). \quad (\text{M5})$$

Here, we consider the term $h_i(t)$ is the intra-coupling strength in the site i and the term $J_i(t)$ is the inter-coupling strength between the site i and $i+1$. So, it is a dimerized Majorana chain with long-range interaction.

Notice that prior to the appearance of topological edge states and domain walls in the dimerized chain, we suppress the interaction terms ($J_z = 0$) and disorders. Indeed, the function of introducing disorders is mainly to create domain wall excitations in the chain by purposes, and that of the small interaction is to add the renormalized kink-kink interaction between DWs in order to dephase the isolated DWs product many-body state into a fully-entangled many-body state. The corresponding Kitaev model for the clear, noninteracting spin model is then given by

$$\bar{H} = -i\bar{J} \sum_{i=1}^{N-1} \gamma_{2i} \gamma_{2i+1} - i\bar{h} \sum_{i=1}^N \gamma_{2i} \gamma_{2i-1}. \quad (\text{M6})$$

This is an analogy of the celebrated SSH model in the Majorana sublattice basis. The Majorana dimerization occurs at $|\bar{J}| \neq |\bar{h}|$. If $|\bar{J}| > |\bar{h}|$, two unpaired Majorana zero modes appear at the ends ($i = 1$, and $2N + 1$), corresponding to the Z_2 breaking ferromagnetic phase in the original Ising model (M1). If $|\bar{J}| < |\bar{h}|$, the ground state will be trivially gapped, corresponding to the paramagnetic phase.

Different from Khemani et al.'s drive protocol [13], our driven parameters in the setting are continuously configured as

$$\begin{aligned} \bar{J}(t) &= \kappa_0 + \delta\kappa_0 + \delta\kappa_1 \cos(\omega t + \phi), \\ \bar{h}(t) &= -(\kappa_0 - \delta\kappa_0 - \delta\kappa_1 \cos(\omega t + \phi)). \end{aligned} \quad (\text{M7})$$

We can rewrite the time-periodic Hamiltonian (M6) into the Majorana SSH-type

$$\bar{H}(t) = -i \sum_{i=1}^{2N-1} [\kappa_0 + (-1)^i (\delta\kappa_0 + \delta\kappa_1 \cos(\omega t + \phi))] \gamma_i \gamma_{i+1}. \quad (\text{M8})$$

We can rewrite (M8) into the anti-symmetric skew-Hermitian matrix form $H = -\frac{i}{2} \sum_{i,j=1}^{2N-1} A_{i,j} \gamma_i \gamma_j$, and numerically solve its quasi-energy spectrum. We address that it shares the similar quasi-energy spectrum of the driven SSH model, as we studied in our waveguide arrays.

Floquet theory and quasi-energy spectrum - For a time-dependent system, the time-evolution of the system is governed by the Schrödinger equation ($\hbar = 1$)

$$i\partial_t|\psi(t)\rangle = H(t)|\psi(t)\rangle, \quad (\text{M9})$$

where $|\psi(t)\rangle = U(t, t_0)|\psi(t_0)\rangle$ is the state of the system at t and $|\psi(t_0)\rangle$ is the state of the system at t_0 . The time evolution operator $U(t, t_0)$ is the solution of the Cauchy problem $i\partial_t U(t, t_0) = H(t)U(t, t_0)$, with the initial value $U(t_0, t_0) = 1$. It can be expressed as

$$U(t, t_0) = \hat{T} e^{-i \int_{t_0}^t H(t') dt'}$$

where \hat{T} is the time-ordering operator. In order to numerically calculate, we can divide the evolution operation into infinite series

$$U(t, t_0) = \lim_{\Delta t \rightarrow 0} e^{-iH(t-\Delta t)\Delta t} e^{-iH(t-2\Delta t)\Delta t} \dots e^{-iH(\Delta t)\Delta t} e^{-iH(0)\Delta t}, \quad (\text{M10})$$

and then we can obtain the dynamic evolution of the time-dependent system (Fig. 3a).

For a periodically driven system with the drive period T , the Hamiltonian of the system has the discrete time-translation symmetry $H(t+T) = H(t)$. The Floquet theorem states that the solution of the Schrödinger equation of the periodically driven system has the form of [54, 55]

$$|\psi_n(t)\rangle = e^{-i\epsilon_n t} |u(t)\rangle, |u_n(t)\rangle = |u_n(t+T)\rangle, \quad (\text{M11})$$

where $|\psi_n(t)\rangle$ is the Floquet state, $|u_n(t)\rangle = |u_n(t+T)\rangle$ is the periodic Floquet mode, and ϵ_n is the quasienergy. Considering the time periodicity, the time evolution operator of the system can be written as $U(t, t_0) = U(t, t_0 + nT)[U(t_0 + T, t_0)]^n$, where $U(t_0 + T, t_0)$ is the Floquet operator defined over one driving period.

Through the Floquet operator, we can define a time-independent effective Floquet Hamiltonian $U(t_0 + T, t_0) = e^{-iH_F[t_0]T}$, where t_0 is the Floquet gauge. By diagonalizing the effective Hamiltonian with the driven tight-binding Hamiltonian,

$$H_{F[t_0]} = \frac{i}{T} \log U(t_0 + T, t_0), \quad (\text{M12})$$

we can calculate the quasienergy spectrum and the Floquet eigenstates, as shown in Fig. 2, in which the gauge $t_0 = 0$, and the quasienergy (ϵ) modulo $2\pi/T$ is confined in the Floquet Brillouin zone.

0- and π -gap invariants - In order to fully characterize the topological properties of the Floquet system by the gap invariants [53], we consider the micromotion operator

$$V(t, t_0) = U(t, t_0) e^{iH_F[t_0](t-t_0)}, \quad (\text{M13})$$

which describes the dynamic evolution within one driving cycle. Under the periodic boundary condition, the Hamiltonian of the driven SSH model in momentum space can be written as

$$H(k, t) = (\kappa_0 + \delta\kappa_0 + \delta\kappa(t) + (\kappa_0 - \delta\kappa_0 - \delta\kappa(t)) \cos(k)) \sigma_x + (\kappa_0 - \delta\kappa_0 - \delta\kappa(t)) \sin(k) \sigma_y, \quad (\text{M14})$$

where $\delta\kappa(t) = \delta\kappa_1 \cos(\omega t)$ and $T = 2\pi/\omega$ is the driving period. The Hamiltonian has chiral symmetry, which is defined as the unitary chiral operator $\Gamma = \sigma_z$,

$$\Gamma H(t, k) \Gamma^{-1} = -H(-t, k), \quad (\text{M15})$$

and the chiral symmetry has the constraint on the micromotion operator $\Gamma V_{\epsilon T}(t, k) \Gamma^{-1} = -V_{-\epsilon T}(-t, k) e^{i2\pi t/T}$. For zero modes, $\epsilon = 0$ and $t = T/2$, we note that $\Gamma V_0(T/2, k) \Gamma^{-1} = -V_0(T/2, k)$, which is anti-diagonal in the chiral basis [53],

$$V_0(T/2, k) = \begin{pmatrix} 0 & V_0^+ \\ V_0^- & 0 \end{pmatrix}. \quad (\text{M16})$$

The chiral invariant is defined by

$$G_0 = \frac{i}{2\pi} \int_{-\pi}^{\pi} \text{tr}((V_0^+)^{-1} \partial_k V_0^+) dk. \quad (\text{M17})$$

For π modes, $\epsilon = \pi/T$ and $t = T/2$, we get that $\Gamma V_{\pi}(T/2, k) \Gamma^{-1} = V_{\pi}(T/2, k)$, which is diagonal in the chiral basis,

$$V_{\pi}(T/2, k) = \begin{pmatrix} V_{\pi}^+ & 0 \\ 0 & V_{\pi}^- \end{pmatrix}. \quad (\text{M18})$$

The chiral invariant is defined by

$$G_{\pi} = \frac{i}{2\pi} \int_{-\pi}^{\pi} \text{tr}((V_{\pi}^+)^{-1} \partial_k V_{\pi}^+) dk. \quad (\text{M19})$$

As a result, we find that for driven SSH Hamiltonian (M14), the invariant $G_{0(\pi)} = 1$ corresponds to the Floquet eigenstates at the quasi-energy $0(\pi)$ -gap, while $G_{0(\pi)} = 0$ to no such an eigenstate.

Reference:

- [1] J. Zhang, P. W. Hess, A. Kyprianidis, P. Becker, A. Lee, J. Smith, G. Pagano, I. D. Potirniche, A. C. Potter, A. Vishwanath, N. Y. Yao, and C. Monroe, Observation of a discrete time crystal. *Nature* 543, 217 (2017).
- [2] S. Choi, J. Choi, R. Landig, G. Kucsko, H. Zhou, J. Isoya, F. Jelezko, S. Onoda, H. Sumiya, V. Khemani, C. von Keyserlingk, N. Y. Yao, E. Demler, and M. D. Lukin, Observation of discrete time-crystalline order in a disordered dipolar many-body system. *Nature* 543, 221 (2017).
- [3] S. Autti, V. B. Eltsov, and G. E. Volovik, Observation of a time quasicrystal and its transition to a superfluid time crystal. *Phys. Rev. Lett.* 120, 215301 (2018).
- [4] J. Smits, L. Liao, H. T. C. Stoof, and P. van der Straten, Observation of a space-time crystal in a superfluid quantum gas. *Phys. Rev. Lett.* 121, 185301 (2018).
- [5] J. Rovny, R. L. Blum, and S. E. Barrett, Observation of discrete-time-crystal signatures in an ordered dipolar many-body system. *Phys. Rev. Lett.* 120, 180603 (2018).
- [6] S. Pal, N. Nishad, T. S. Mahesh, and G. J. Sreejith, Temporal order in periodically driven spins in star-shaped clusters. *Phys. Rev. Lett.* 120, 180602 (2018).
- [7] F. Wilczek, Quantum time crystals. *Phys. Rev. Lett.* 109, 160401 (2012).
- [8] A. Shapere, and F. Wilczek, Classical time crystals. *Phys. Rev. Lett.* 109, 160402 (2012).
- [9] V. K. Kozin, and O. Kyriienko, Quantum time crystals from Hamiltonians with long-range interactions. *Phys. Rev. Lett.* 123, 210602 (2019).
- [10] P. Bruno, Impossibility of Spontaneously Rotating Time Crystals: A No-go Theorem. *Phys. Rev. Lett.* 111, 070402 (2013).
- [11] H. Watanabe, and M. Oshikawa, Absence of quantum time crystals. *Phys. Rev. Lett.* 114, 251603 (2015).
- [12] K. Sacha, Modeling spontaneous breaking of time-translation symmetry. *Phys. Rev. A* 91, 033617 (2015).
- [13] V. Khemani, A. Lazarides, R. Moessner, and S. L. Sondhi, Phase structure of driven quantum systems. *Phys. Rev. Lett.* 116, 250401 (2016).
- [14] D. V. Else, B. Bauer, and C. Nayak, Floquet time crystals. *Phys. Rev. Lett.* 117, 090402 (2016).
- [15] N. Y. Yao, A. C. Potter, I.-D. Potirniche, and A. Vishwanath, Discrete time crystals: rigidity, criticality, and realizations. *Phys. Rev. Lett.* 118, 030401 (2017).
- [16] K. Sacha, and J. Zakrzewski, Time crystals: a review. *Reports on Progress in Physics*, 81, 016401 (2017).
- [17] N. Y. Yao, and C. Nayak, Time crystals in periodically driven systems. *Phys. Today* 71, 9, 40 (2018).
- [18] V. Khemani, R. Moessner, and S. L. Sondhi, A brief history of time crystals. arXiv:1910.10745 (2019).
- [19] D. V. Else, C. Monroe, C. Nayak, and N. Y. Yao, Discrete time crystals. *Annu. Rev. Condens. Matter Phys.* 11, 467 (2020).
- [20] Z. Gong, R. Hamazaki, and M. Ueda, Discrete time-crystalline order in cavity and circuit QED systems. *Phys. Rev. Lett.* 120, 040404 (2018).

- [21] F. Iemini, A. Russomanno, J. Keeling, M. Schirò, M. Dalmonte, and R. Fazio, Boundary Time Crystals. *Phys. Rev. Lett.* 121, 035301 (2018).
- [22] B. Huang, Y. H. Wu, and W. V. Liu, Clean Floquet Time Crystals: Models and Realizations in Cold Atoms. *Phys. Rev. Lett.* 120, 110603 (2018).
- [23] A. Pizzi, J. Knolle, and A. Nunnenkamp, Period-n Discrete Time Crystals and Quasicrystals with Ultracold Bosons. *Phys. Rev. Lett.* **123**, 150601 (2019).
- [24] R. W. Bomantara and J. Gong, Simulation of Non-Abelian Braiding in Majorana Time Crystals. *Phys. Rev. Lett.* 120, 230405 (2018).
- [25] A. Chew, D. F. Mross, and J. Alicea, Time-Crystalline Topological Superconductors. *Phys. Rev. Lett.* 124, 096802 (2020).
- [26] R. R. Wang, B. Xing, G. G. Carlo, and D. Poletti, Period doubling in period-one steady states. *Phys. Rev. E* 97, 020202(2018).
- [27] B. van der Pol, and J. van der Mark, Frequency Demultiplication. *Nature*, 120, 363 (1927).
- [28] P. Nurwantoro, R. W. Bomantara, and J. Gong, Discrete time crystals in many-body quantum chaos. *Phys. Rev. B* 100, 214311 (2019).
- [29] N. Y. Yao, C. Nayak, L. Balents, and M. P. Zaletel, Classical discrete time crystals. *Nat. Phys.* 16, 438 (2020).
- [30] T. L. Heugel, M. Oscity, A. Eichler, O. Zilberberg, and R. Chitra, Classical many-body time crystals. *Phys. Rev. Lett.* 123, 124301 (2019).
- [31] A. Lazarides, S. Roy, F. Piazza, and R. Moessner, Time crystallinity in dissipative Floquet systems. *Phys. Rev. Research*, 2, 022002 (2020).
- [32] A. Riera-Campeny, M. Moreno-Cardoner, and A. Sanpera, Time crystallinity in open quantum systems. *Quantum*, 4, 270 (2020).
- [33] K. Mizuta, K. Takasan, M. Nakagawa, and N. Kawakami, Spatial-Translation-Induced Discrete Time Crystals, *Phys. Rev. Lett.* 121, 093001 (2018).
- [34] P. Matus, and K. Sacha. Fractional time crystals. *Phys. Rev. A* 99, 033626 (2019).
- [35] H. Zhao, F. Mintert, and J. Knolle, Floquet time spirals and stable discrete-time quasicrystals in quasiperiodically driven quantum many-body systems. *Phys. Rev. B* 100, 134302 (2019).
- [36] E. Lustig, Y. Sharabi, and M. Segev. Topological aspects of photonic time crystals. *Optica*, 5, 1390 (2018).
- [37] K. Giergiel, A. Dauphin, M. Lewenstein, J. Zakrzewski, and K. Sacha, Topological time crystals, *New J. Phys.* 21, 052003 (2019).
- [38] Y. Pan and B. Wang, Time-crystalline phases and period-doubling oscillations in one-dimensional Floquet topological insulators. *Phys. Rev. Research*, 2, 043239 (2020).
- [39] M. Benito, A. Gómez-León, V. M. Bastidas, T. Brandes, and G. Platero, Floquet engineering of long-range p-wave superconductivity. *Phys. Rev. B*, 90, 205127 (2014).
- [40] A. Russomanno, and E. G. Dalla Torre, Spin and topological order in a periodically driven spin chain. *Phys. Rev. B*, 96, 045422 (2017).
- [41] T. Liu, D. J. Shabani, and A. Mitra, Floquet Majorana zero and π modes in planar Josephson junctions. *Phys. Rev. B*, 99, 094303 (2019).
- [42] O. Shtanko, and R. Movassagh, Unitary Subharmonic Response and Floquet Majorana Modes. *Phys. Rev. Lett.* 125, 086804 (2020).

- [43] M. Z. Hasan and C. L. Kane, *Colloquium: Topological insulators*, *Rev. Mod. Phys.* 82, 3045 (2010).
- [44] X.-L. Qi and S.-C. Zhang, Topological insulators and superconductors, *Rev. Mod. Phys.* 83, 1057 (2011).
- [45] M. C. Rechtsman, J. M. Zeuner, Y. Plotnik, Y. Lumer, D. Podolsky, F. Dreisow, S. Nolte, M. Segev and A. Szameit, Photonic Floquet topological insulators, *Nature*, 496, 196-200 (2013).
- [46] L. Lu, J. D. Joannopoulos, and M. Soljačić, Topological photonics, *Nat. Photon.* 8, 821 (2014).
- [47] T. Ozawa, H. M. Price, A. Amo, N. Goldman, M. Hafezi, L. Lu, M. C. Rechtsman, D. Schuster, J. Simon, O. Zilberberg and I. Carusotto, Topological photonics, *Rev. Mod. Phys.* 91, 015006 (2019).
- [48] D. A. Abanin, E. Altman, I. Bloch, and M. Serbyn, *Colloquium: Many-body localization, thermalization, and entanglement*, *Rev. Mod. Phys.* 91, 021001 (2019).
- [49] E. Altman, and R. Vosk, Universal dynamics and renormalization in many-body-localized systems, *Annu. Rev. Condens. Matter Phys.* 6, 383 (2015).
- [50] R. Nandkishore, and D. A. Huse, Many-body localization and thermalization in quantum statistical mechanics, *Annu. Rev. Condens. Matter Phys.* 6, 15 (2015).
- [51] M. S. Rudner, N. H. Lindner, E. Berg, and M. Levin, Anomalous Edge States and the Bulk-Edge Correspondence for Periodically Driven Two-Dimensional Systems, *Phys. Rev. X* 3, 031005 (2013).
- [52] V. Dal Lago, M. Atala, and L. F. Torres, Floquet topological transitions in a driven one-dimensional topological insulator. *Phys. Rev. A* 92, 023624 (2015).
- [53] M. Fruchart, Complex classes of periodically driven topological lattice systems. *Phys. Rev. B* 93, 115429 (2016).
- [54] M. Bukov, L. D'Alessio, and A. Polkovnikov, Universal high-frequency behavior of periodically driven systems: from dynamical stabilization to Floquet engineering. *Advances in Physics*, 64, 139 (2015).
- [55] A. Eckardt, and E. Anisimovas, High-frequency approximation for periodically driven quantum systems from a Floquet-space perspective. *New J. Phys.* 17, 093039 (2015).
- [56] W. Su, J. R. Schrieffer, and A. J. Heeger, Solitons in polyacetylene. *Phys. Rev. Lett.* 42, 1698 (1979).
- [57] X. Shen, T. J. Cui, D. Martin-Cano, and F. J. Garcia-Vidal, Conformal surface plasmons propagating on ultrathin and flexible films, *Proceedings of the National Academy of Sciences*, 110, 40 (2013).
- [58] H. F. Ma, X. Shen, Q. Cheng, W. X. Jiang, and T. J. Cui, Broadband and high-efficiency conversion from guided waves to spoof surface plasmon polaritons, *Laser & Photonics Reviews*, 8, 146 (2014).
- [59] Q. Cheng, Y. Pan, H. Wang, C. Zhang, D. Yu, A. Gover, and S. Zhu, Observation of Anomalous π Modes in Photonic Floquet Engineering, *Phys. Rev. Lett.* 122, 173901 (2019).
- [60] Q. Cheng, T. Chen, D. Yu, Y. Liao, J. Xie, X. Zang, P. Shen, and Y. Pan, Flexibly designed spoof surface plasmon waveguide array for topological zero-mode realization, *Optics Express*, 26, 31636 (2018).

- [61] T. Vachaspati, Kinks and domain walls: An introduction to classical and quantum solitons, Cambridge University Press (2006).
- [62] D. Smirnova, D. Leykam, Y. Chong, and Y. Kivshar, Nonlinear topological photonics, *Applied Physics Reviews*, 7, 021306 (2020).

Figures:

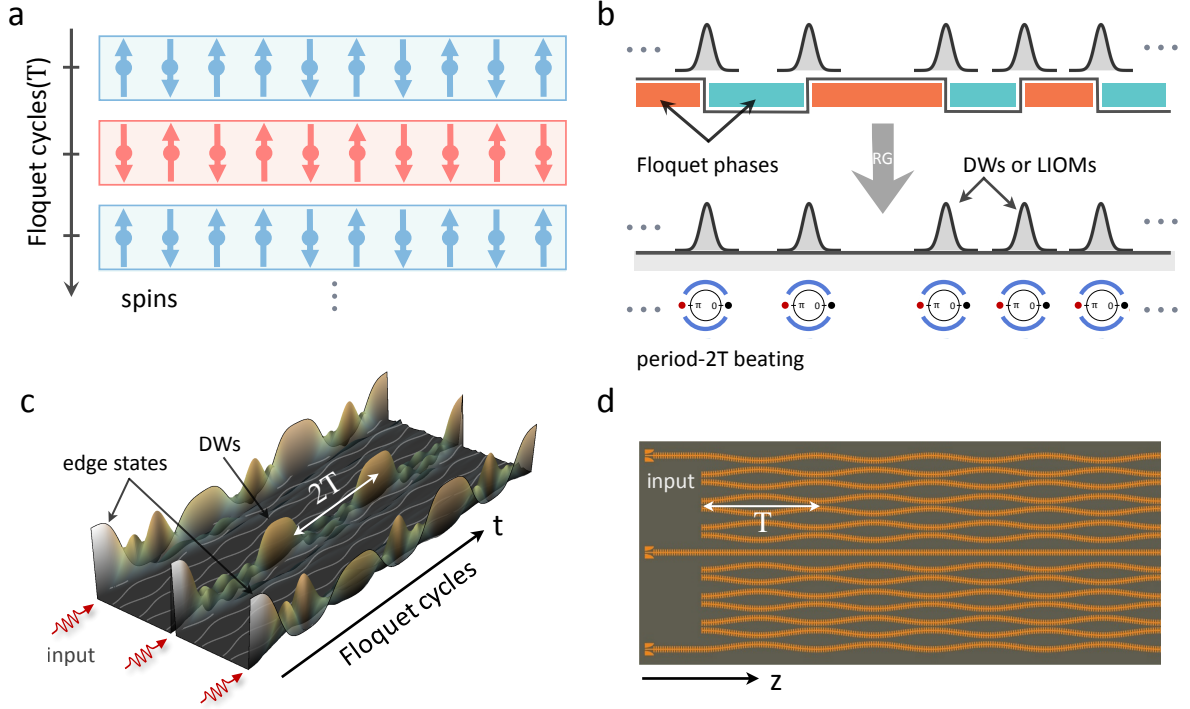


Fig. 1: Illustration of period-2T Floquet time-crystalline phases in topologically-protected single-particle pictures. (a) Many-body-localization-enabled Floquet time crystal on a spin chain. (b) Emergence of domain walls or local integrals of motions (LIOMs) in one-dimensional disordered Floquet phases. The superposition of Floquet topological invariants zero and π modes of the renormalized low-lying DW excitations offers the rigid period-doubling beating as a time-crystalline clock. (c) The schematic diagram of DWs and edge states stroboscopic evolutions on a chain of (e.g., spins, atoms, and waveguides) with a periodically-driven protocol, demonstrating the pertinent period-2T beating. (d) Schematic diagram of the curved waveguide array structure with three field inputs. In particular, the central waveguide is straight for constructing the domain wall.

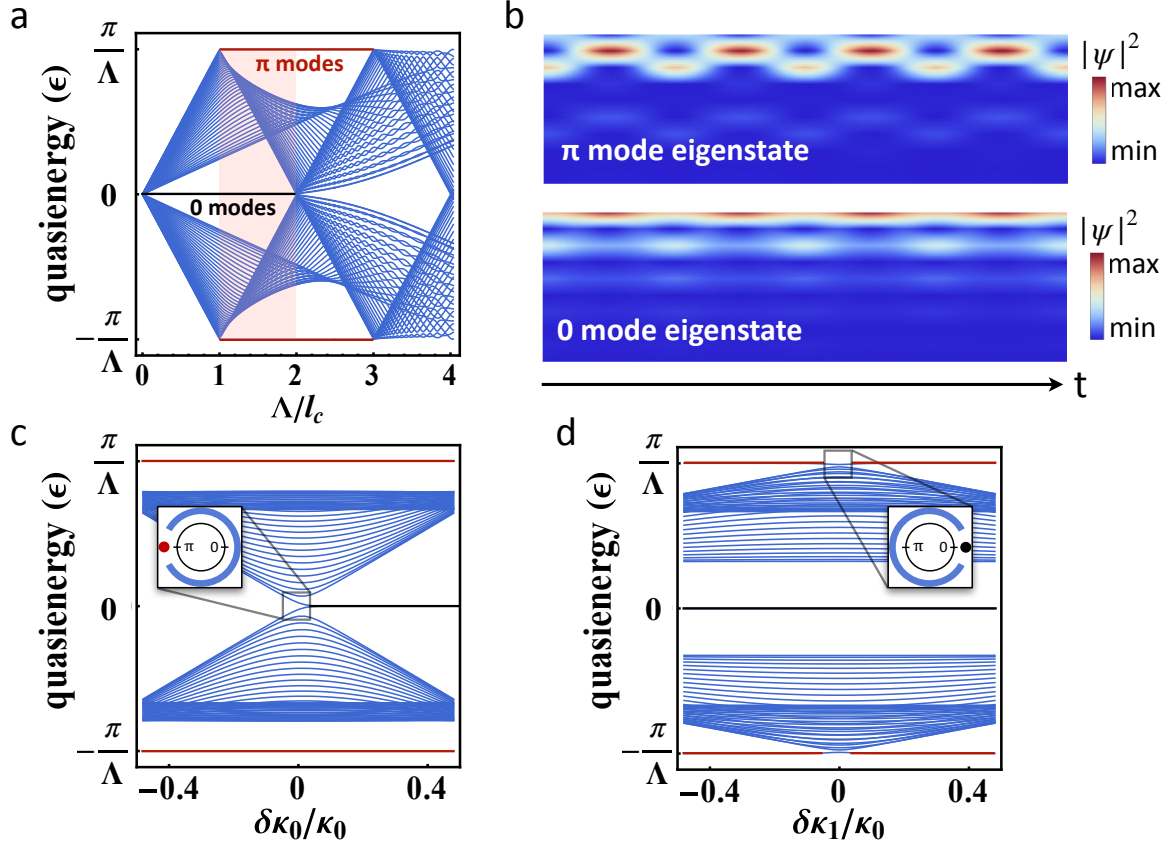


Fig. 2: Quasienergy spectrum of photonic FTC and micromotion eigenstates of topological 0 and π modes. (a) Quasienergy band as a function of the curving period (Λ). (b) The micromotions of π mode and 0 mode eigenstates in four Floquet cycles ($4T$). The Floquet cycle T is mapped to the curving period Λ . The two Floquet topological modes coexist in the driven condition $\Lambda/l_c \in (1, 2)$, and the coupling length $l_c = \pi/2\kappa_0$. The parameters are $\kappa_0 = 0.25, \delta\kappa_0 = 0.06, \delta\kappa_1 = 0.12$. (c) The 0-gap as a function of global dimerization $\delta\kappa_0/\kappa_0$, closed at $\delta\kappa_0/\kappa_0 = 0$. (d) The π -gap as a function of time-period dimerization $\delta\kappa_1/\kappa_0$, closed at $\delta\kappa_1/\kappa_0 = 0$. The insets of (c) and (d) are the quasienergy band of the sole existence of π modes and 0 modes at $\Lambda/l_c = 4/3$, respectively.

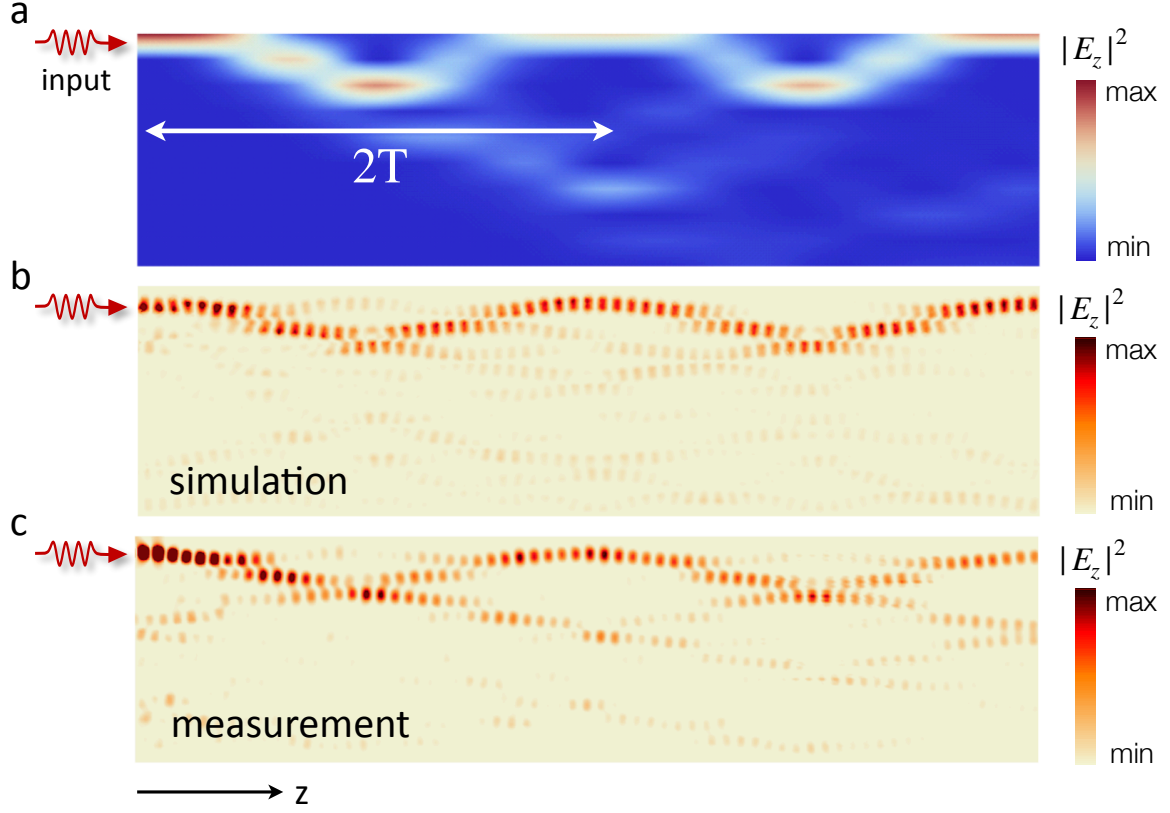


Fig. 3: Observation of period- $2T$ oscillation in photonic Floquet simulator. (a) Theoretical calculation based on the Floquet evolution operator. (b) FEM simulation based on COMSOL. (c) Near-field measurement based on the fabricated array sample. The field was input from the edge of the waveguide array (waveguide number $N = 10$) with the input frequency 17.0 GHz for simulations and 16.9 GHz for experiments. The length of the simulator is $L = 400 \text{ mm}$. The theory, simulation and experiment are perfectly in agreement with each other. The corresponding parameters are given in the main text.

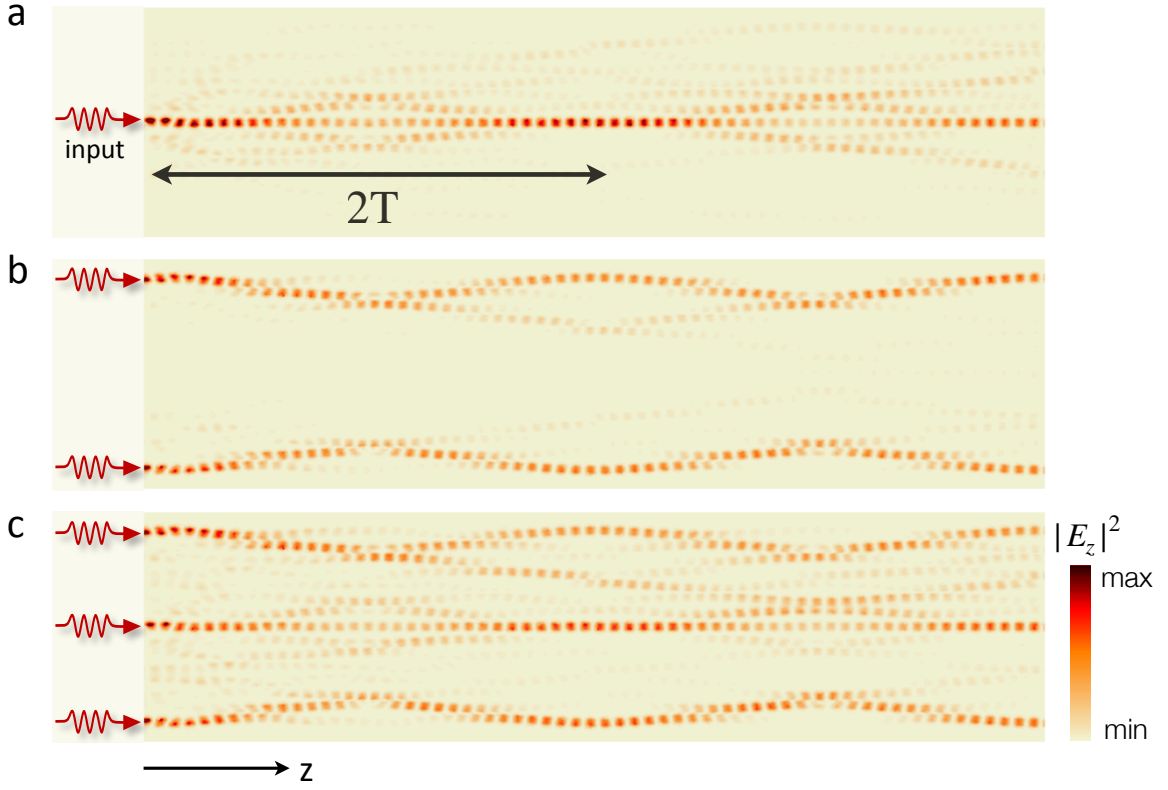


Fig. 4: Comparison between single-particle and many-body time crystals with the different inputs from edge states and a central domain wall. (a) The near-field evolution with two edge-state inputs. (b) The near-field evolution with the central domain-wall input. (c) The near-field evolution with combine edge-state and the domain-wall inputs. The simulations based on the samples (Fig. 1d) demonstrate the photonic period- $2T$ oscillation. The structural parameters are $N = 15$, $L = 400 \text{ mm}$, $\Lambda = 100 \text{ mm}$ and the input frequency is 17.0 GHz .

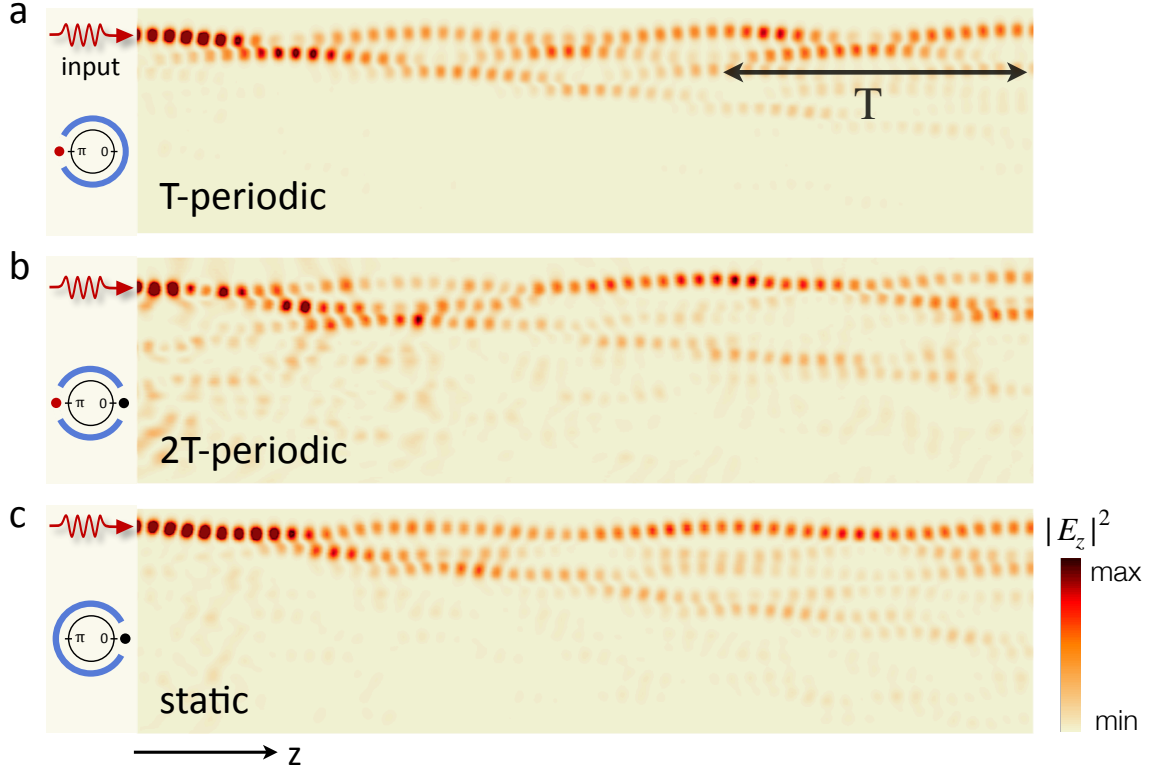


Fig. 5: Observation of topological phase transition in Floquet simulators. By altering the ratio between the periodic and global dimerization spacing, we can open the corresponding quasienergy gap as shown in the insets. (a) For $G_{min1} = 0.9 \text{ mm}$, $G_{min2} = 0.9 \text{ mm}$, only π mode exists, and the photonic system exhibits the period- T oscillation when the π mode is excited. (b) For $G_{min1} = 1.9 \text{ mm}$, $G_{min2} = 0.9 \text{ mm}$, 0 and π modes coexist, and the system exhibits the period- $2T$ oscillation when the two modes are excited simultaneously. (c) For $G_{min1} = 2.3 \text{ mm}$, $G_{min2} = 0.9 \text{ mm}$, only 0 mode is effectively excited. The system exhibits the non-driven static behavior. Note that the input frequency is 17.4 GHz , the array length is $L = 300 \text{ mm}$, and the period is $\Lambda = 100 \text{ mm}$, so the Floquet cycles is $3T$.

Supplementary Material:

Photonic Floquet time crystals

Bing Wang^{†,1}, Jiaqi Quan^{†,2}, Jianfei Han³, Xiaopeng Shen^{*,3}, Hongwei Wu^{*,2}, and Yiming Pan^{*,4}

1. National Laboratory of Solid State Microstructures and School of Physics, Nanjing University, Nanjing 210093, CHINA
2. School of Mechanics and Photoelectric Physics, Anhui University of Science and Technology, Huainan 232001, CHINA
3. School of Materials Science and Physics, China University of Mining and Technology, Xuzhou 221116, CHINA
4. Physics Department and Solid State Institute, Technion, Haifa 32000, ISRAEL

1. Experiment setup

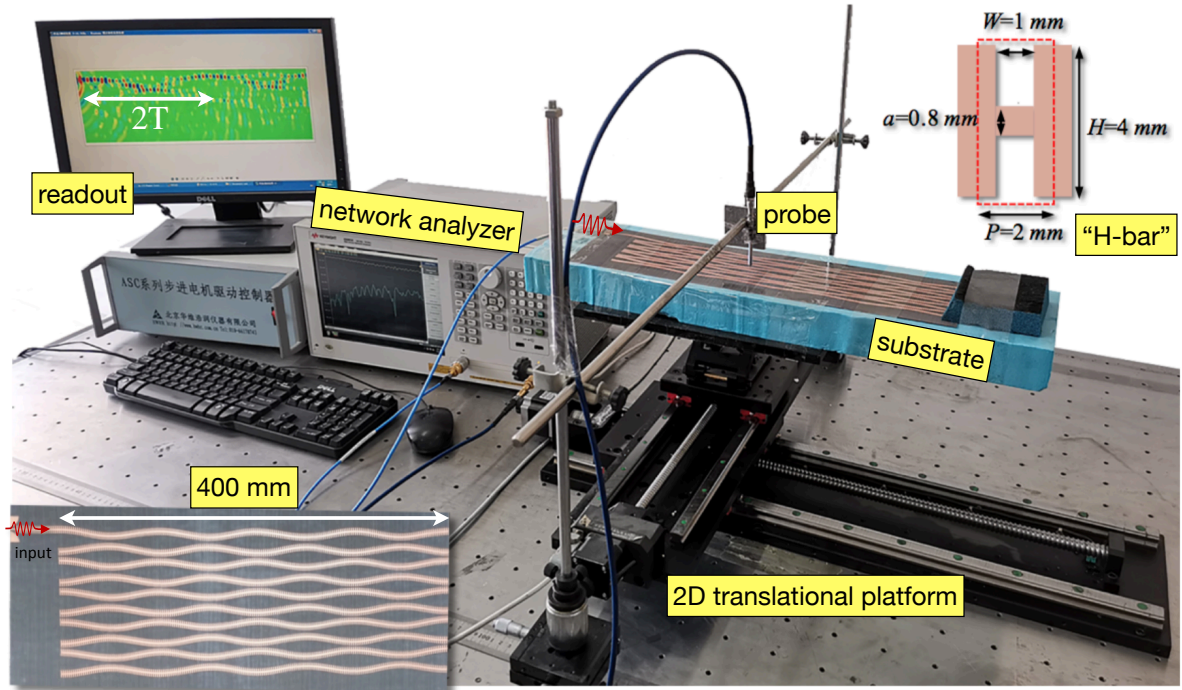


Fig. S1: Photograph of the microwave near-field experiment platform, including vector network analyzer (KeysightE5063A), two-dimensional translation platform, and platform controller. The sample is pasted on a foam whose dielectric constant is near 1 and ‘influence’ on the sample can be ignored. The foam is placed on the movable platform bottom plate which can move in X -, and Y -directions controlled by the mechanical stage. One port of the vector network analyzer is connected to the feed coaxial line to provide the microwave source signal, and the other port is connected to the coaxial detection probe (the tip). The probe is fixed on the fixed frame to mapping the Z component of the electric field in the plane 1mm above the sample. The field density information can be observed by a specific computer program. The lower left inset shows the enlarged sample photograph.

2. Reconstructions of coupling profiles with two waveguides in simulation

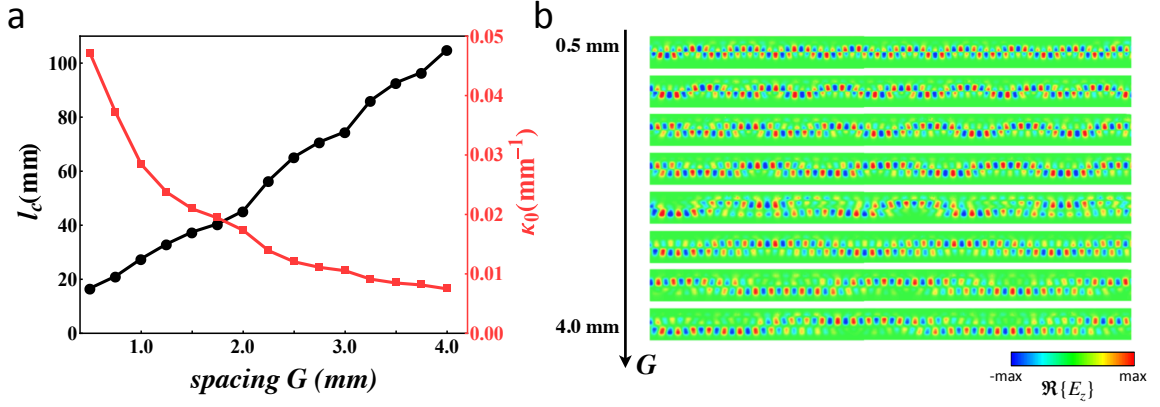


Fig. S2: Reconstruction of coupling profiles from the simulation of two coupled waveguides. (a) The coupling length l_c and the coupling strength κ_0 as a function with the spacing (G) of the adjacent waveguides. The relation between the coupling length and the coupling strength is given by $l_c = \pi/2\kappa_0$. (b) The simulation results of the electric field propagation between two coupled waveguides. The spacing of the adjacent waveguides varies from 0.5 mm to 4.0 mm. The coupling length can be estimated by the effective distance of the input field fully propagating from one waveguide to the next. Note that the waveguide length is 400 mm and the input frequency used for simulation is 17.0 GHz.

3. Floquet topological phase transition in driven Su-Schrieffer-Heeger setup

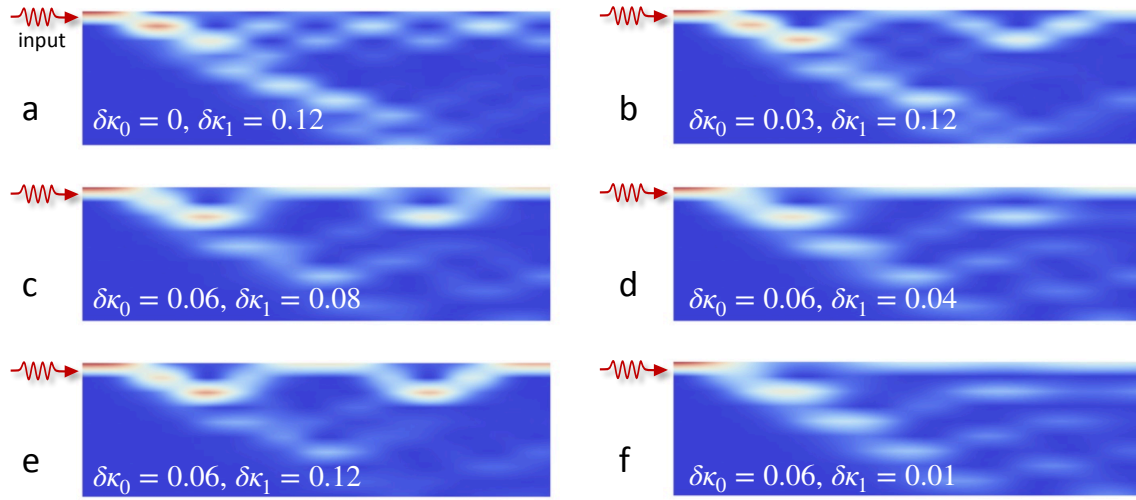


Fig. S3: The theoretical results for the Floquet topological phase transition with changing the dimerized coupling strengths. (a) The only π mode phase with $\delta\kappa_0 = 0, \delta\kappa_1 \neq 0$. (b-e) The time crystalline phase coexistence with $\delta\kappa_0 \neq 0, \delta\kappa_1 \neq 0$. (f) The 0 mode phase with $\delta\kappa_0 \neq 0, \delta\kappa_1 = 0$. The theoretical results are calculated with 80 waveguides and $\omega/\Delta = 0.75, \kappa_0/\Delta = 0.25, \Delta = 1$ (the bandwidth). Note that for demonstration in high resolution, only the first ten waveguides of the array are plotted in four Floquet cycles ($4T$).

4. Floquet topological phase transition in photonic Floquet simulator

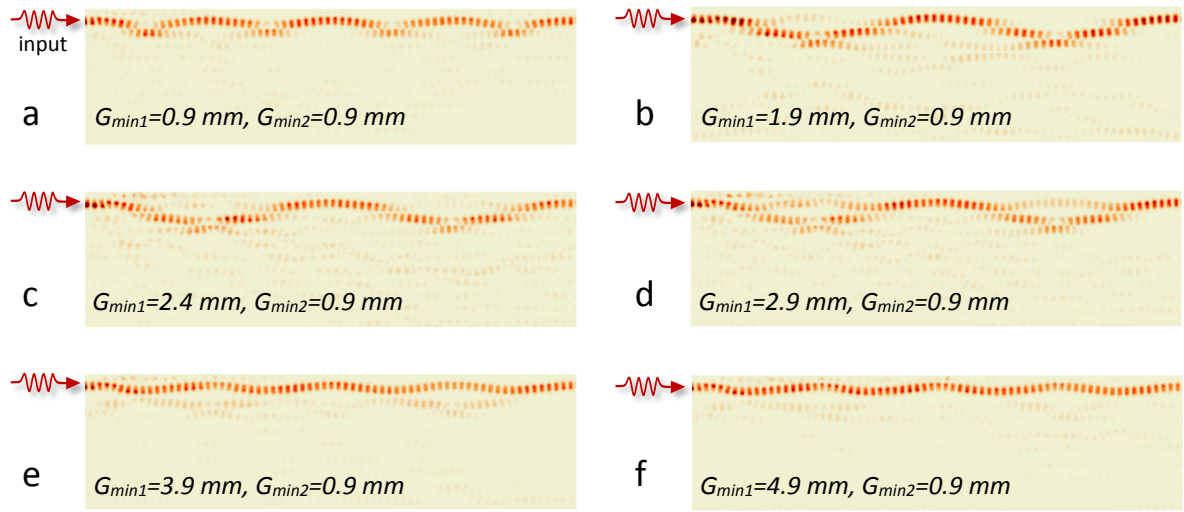


Fig. S4: The simulation results for the Floquet topological phase transition with changing the spacing of the adjacent waveguides. (a) π mode phase. (b-d) Time crystalline phase. (e, f) 0 mode phase. There are ten waveguides in an array and the length of the array is $L = 400 \text{ mm}$ with the curving period 100 mm . The input frequency used for simulation is 17.0 GHz .

5. Period- $2T$ oscillation with different input frequencies in simulation

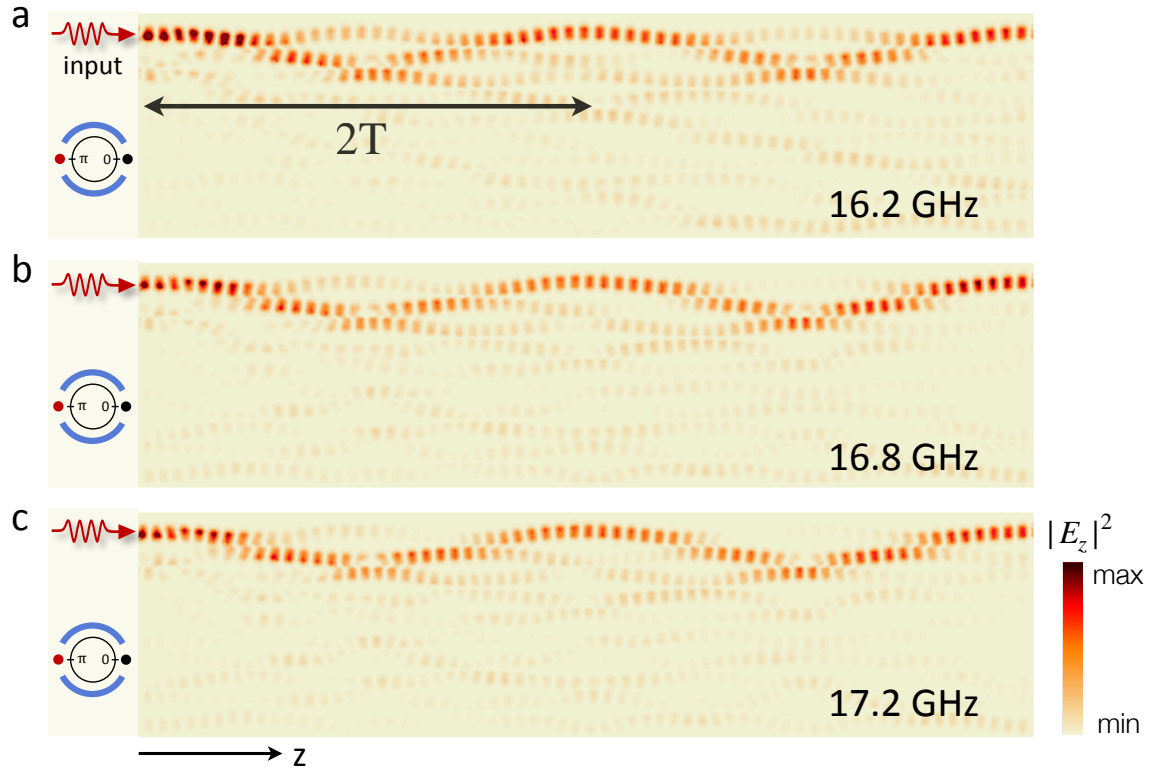


Fig. S5: The simulation results for the period- $2T$ oscillation with different input frequencies. (a) 16.2 GHz. (b) 16.8 GHz. (c) 17.2 GHz. There are ten waveguides in an array and the length of the array is $L = 400 \text{ mm}$ with the curving period 100 mm . The corresponding minimal spacing of the adjacent waveguides are $G_{min1} = 1.9 \text{ mm}$, $G_{min2} = 0.9 \text{ mm}$.

6. Period- $2T$ oscillation with different input frequencies in experiment

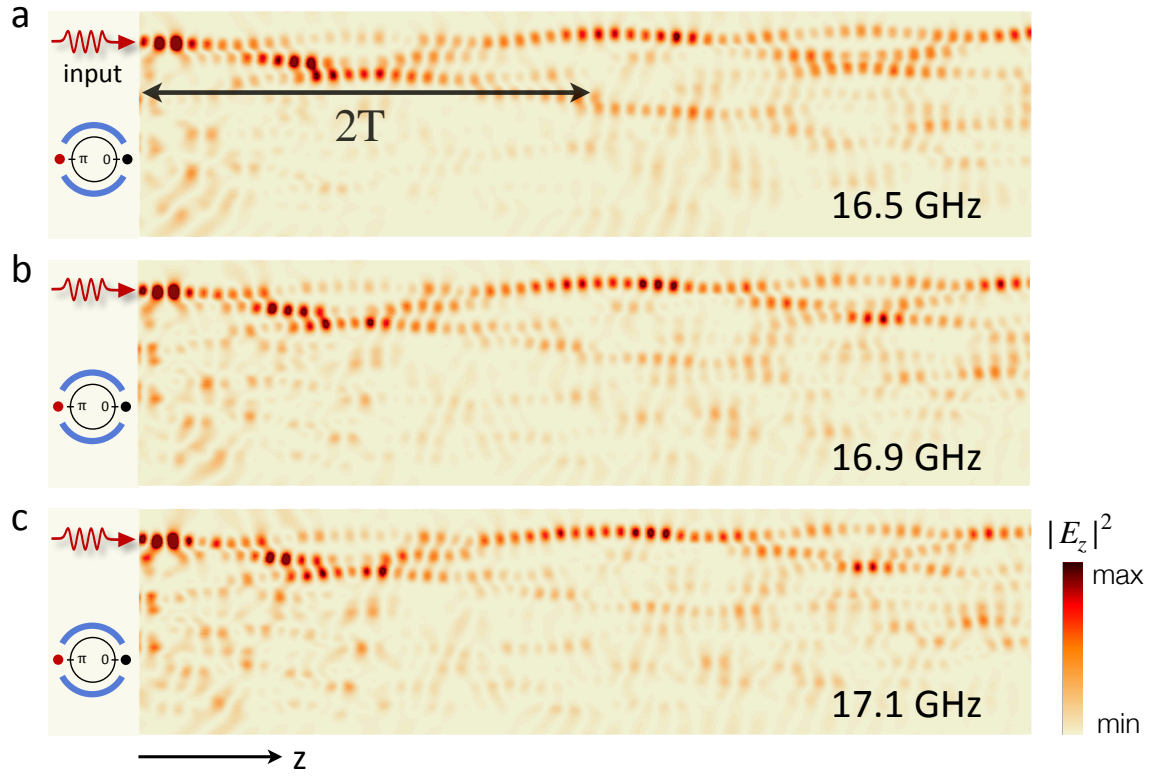


Fig. S6: The measurement results for the period- $2T$ oscillation with different input frequencies. (a) 16.5 GHz. (b) 16.9 GHz. (c) 17.1 GHz. There are 10 waveguides and the waveguides length is 400 mm with one period length 100 mm. The minimal spacing of the adjacent waveguides are $G_{min1} = 1.9$ mm, $G_{min2} = 0.9$ mm, as same as Fig. S5.